

Non-thermal X-rays and interstellar gas toward the γ -ray supernova remnant RX J1713.7–3946: Evidence for X-ray enhancement around CO and HI clumps

H. Sano¹, T. Tanaka², K. Torii¹, T. Fukuda¹, S. Yoshiike¹, J. Sato¹, H. Horachi¹, T. Kuwahara¹, T. Hayakawa¹, H. Matsumoto¹, T. Inoue³, R. Yamazaki³, S. Inutsuka¹, A. Kawamura^{1,5}, H. Yamamoto¹, T. Okuda¹, N. Mizuno^{1,4}, T. Onishi^{1,5}, A. Mizuno⁶ and Y. Fukui¹

¹Department of Physics and Astrophysics, Nagoya University, Furo-cho, Chikusa-ku, Nagoya, 464-8601, Japan; sano@a.phys.nagoya-u.ac.jp

²Department of Physics, Kyoto University, Kitashirakawa-oiwake-cho, Sakyo-ku, Kyoto 606-8502, Japan

³Department of Physics and Mathematics, Aoyama Gakuin University, Fuchinobe, Chuou-ku, Sagamihara, 252-5258, Japan

⁴National Astronomical Observatory of Japan, Mitaka, 181-8588, Japan

⁵Department of Astrophysics, Graduate School of Science, Osaka Prefecture University, 1-1 Gakuen-cho, Naka-ku, Sakai, 599-8531, Japan

⁶Solar-Terrestrial Environment Laboratory, Nagoya University, Furo-cho, Chikusa-ku, Nagoya, 464-8601, Japan

Received _____; accepted _____

ABSTRACT

RX J1713.7–3946 is the most remarkable very-high-energy γ -ray supernova remnant which emits synchrotron X-rays without thermal features. We made a comparative study of CO, HI and X-rays in order to better understand the relationship between the X-rays, and molecular and atomic gas. The results indicate that the X-rays are enhanced around the CO and HI clumps on a pc scale but decrease inside the clumps on a 0.1 pc scale. Magnetohydrodynamic numerical simulations of the shock interaction with molecular and atomic gas indicate that the interaction between the shock waves and the clumps excite turbulence which amplifies the magnetic field around the clumps. We suggest that the amplified magnetic field around the CO and HI clumps enhances the synchrotron X-rays and possibly the acceleration of cosmic-ray electrons.

Subject headings: cosmic rays – X-rays: ISM – ISM: supernova remnants – ISM: individual objects (RX J1713.7–3946) – ISM: clouds

1. Introduction

RX J1713.7–3946 is one of the most prominent supernova remnants (SNRs) emitting highest energy radiation covering the γ -rays and X-rays. The SNR is located relatively close to the Galactic center at $(l, b) = (347^\circ 3, -0^\circ 5)$, where contamination by the foreground/background features is heavy at any wavelength. The SNR was not known as a SNR in the radio continuum emission and was discovered in the X-rays by the *ROSAT* (Pfeffermann & Aschenbach 1996). The VHE (very high energy) γ -rays from the SNR were discovered and mapped by the atmospheric Cherenkov telescopes (Enomoto et al. 2002; Aharonian et al. 2004, 2006a,b, 2007). In particular, the H.E.S.S. observations resolved that the γ -rays distribution is shell-like with a diameter of 1° by 0.1-degree diameter PSF (point spread function). Since the γ -rays are detected at an energy range higher than 10 TeV, the cosmic ray (CR) protons producing the γ -rays may reach an energy range above several 100 TeV, if the hadronic mechanism is working. The SNR is therefore an important candidate where the acceleration of the highest energy CR protons is best tested in the Galaxy. It is noteworthy that the X-rays of the SNR are purely non-thermal synchrotron emission; there are only two SNRs except for RX J1713.7–3946, which show such non-thermal X-rays, RX J0852.0–4622 (Vela Jr.) and HESS J1731–347, known to date (e.g., Koyama et al. 1997; Slane et al. 2001; Tian et al. 2010).

The distance of the SNR was under controversy around 2000 (e.g., Koyama et al. 1997; Wang et al. 1997; Slane et al. 1999). It is now well established that the SNR is located at 1 kpc from us as first determined by the radial velocity of the associated CO molecular gas at -7 km s^{-1} in V_{LSR} (Fukui et al. 2003). This distance is confirmed by subsequent observations in X-rays and CO (Cassam-Chenaï et al. 2004; Moriguchi et al. 2005). Moriguchi et al. (2005) showed further details of the $^{12}\text{CO}(J=1-0)$ distribution and confirmed the interacting molecular gas identified by Fukui et al. (2003). Most recently,

Sano et al. (2010, hereafter paper I) presented a comparison with the X-rays for the western rim of the SNR in $^{12}\text{CO}(J=2-1, 4-3)$ transitions, where most prominent mm/sub-mm CO clumps are distributed. These authors found that cloud core named “peak C” is a site of low-mass star formation and is surrounded by X-rays at pc scales, lending a further support for the distance of 1 kpc. Also, a comparison between the distribution of the *Suzaku* X-rays and the CO indicates that the dense cloud core shows an anti-correlation with the X-rays at sub-pc scales. The result suggests that the magnetic field is amplified around the dense cloud cores, leading to bright X-rays. It is noteworthy that the density distribution is generally highly inhomogeneous in the SNR as shown by these CO observations and such inhomogeneity remains to be incorporated fully in treating the interaction of high-energy particles with the interstellar medium (ISM) (Fukui 2008; Zirakashvili & Aharonian 2010), rather than simply assuming the uniform ISM distribution as in the previous works (e.g., Ellison et al. 2010, 2012).

Aiming at better understanding results of X- and γ -ray observations and their relationship with the neutral ISM, we are promoting a comprehensive comparison among the X-rays, the γ -rays and the ISM in γ -ray SNRs (e.g., Paper I; Fukui et al. 2012, hereafter paper II; Yoshiike et al. 2013). Paper II presented an analysis of the interstellar protons both in molecular and atomic forms and showed a good spatial correspondence between the clumpy ISM protons and the VHE γ -rays. This provides a crucial support for the hadronic origin of the γ -rays instead of the leptonic origin. Now, in RX J1713.7–3946, the next step is to establish the connection between the synchrotron X-rays and the ISM distribution. This work is aimed at better understanding the SNR shock-cloud interaction and obtaining a clue to the origin of the distribution of the synchrotron X-rays in the SNR. In the present paper we show a comparison of the spatial distribution among $^{12}\text{CO}(J=2-1)$, H I and X-rays over the whole SNR in order to clarify the relationship between cold dense gas and the high-energy electrons. We will publish a separate paper that deals with a detailed spectral

analysis of the *Suzaku* X-ray results compared with the interstellar gas distribution (Sano et al. 2013b in prep.).

The paper is organized as follows. Section 2 gives the description of the datasets of CO, H_I and X-rays and Section 3 gives the analysis. Section 4 gives discussion and Section 5 the conclusions.

2. Observations and data reductions

2.1. CO

The $^{12}\text{CO}(J=2-1)$ data at 230 GHz were taken with the NANTEN2 4 m telescope in the period from August to November in 2008, and were published in Papers I, II and Maxted et al. (2012). The front end was a 4 K cooled double sideband (DSB) receiver and a typical system temperature was ~ 250 K in the single sideband (SSB) including the atmosphere toward the zenith. The telescope had an angular resolution (FWHM) of $90''$ at 230 GHz. We used an acoustic optical spectrometer has 2048 channels with a bandwidth of 390 km s^{-1} and resolution per channel of 0.38 km s^{-1} . Observations were carried out in the on-the-fly mode with an integration time of 1.0 s or 2.0 s per grid, and provided a Nyquist-sampled $30''$ grid dataset. The ambient temperature load was employed for the intensity calibration. The absolute intensity scale was estimated by observing the Ori KL object [$5^{\text{h}}35^{\text{m}}14^{\text{s}}52; -5^{\circ}22'28''.2$ (J2000)] (Schneider et al. 1998) and the main beam efficiency, η_{mb} , was estimated to be 0.83. The rms noise fluctuations with 1.0 s and 2.0 s integrations were better than 0.66 K and 0.51 K per channel, respectively. The pointing accuracy was estimated to be better than $\sim 15''$ by observing Jupiter every two hours. The image was smoothed with a Gaussian kernel with FWHM of $60''$. The observed area is shown in the Figure 1.

2.2. HI

The 21 cm HI spectral data were taken from the Southern Galactic Plane Survey (SGPS; McClure-Griffiths et al. 2005) with the Australia Telescope Compact Array (ATCA) combined with the 64 m Parkes Radio Telescope. The combined beam size and the grid spacing of the dataset are 2.2 arcmin and $40''$, respectively. Also, the velocity resolution and typical rms noise fluctuations were 0.82 km s^{-1} and 1.9 K, respectively. We applied the correction for the HI self-absorption by following the previous analysis of the cool HI gas without CO emission (see Section 3.3 of Paper II).

2.3. X-rays

We used *Suzaku* archive data of RX J1713.7–3946 taken from Data Archives and Transmission System (DARTS at ISAS/JAXA). The observations performed 15 pointings toward the main features and 2 OFF pointings of RX J1713.7–3946 and were published by Takahashi et al. (2008) and Tanaka et al. (2008) expect for the 4 pointings observed in 2010 February. Previous and current observations are summarized in Table 1, and the FoV of each observation is shown in Figure 1. Active detector systems aboard the *Suzaku* satellite are the X-ray Imaging Spectrometer (XIS; Koyama et al. 2007) and the Hard X-ray Detector (HXD). The XIS consists of four CCD cameras placed at the foci of X-ray Telescopes (XRTs; Serlemitsos et al. 2007). We analyzed only XIS data in the present paper. The spaced-row charge injection (SCI; Nakajima et al. 2008, Uchiyama et al. 2009) was used in the latter 4 pointings (see also Table 1). Unfortunately, XIS 2 was on closed access since 2006 November 9, possibly owing to a micrometeorite damage. XIS 0 showed an anomaly in Segment A on 2009 June 23. Thus, for the data in the latter 4 pointings we used XIS 0 (expect for Segment A), XIS 1 and XIS 3. We used “cleaned event files” processed and screened by versions 2.0 or 2.4 *Suzaku* pipeline depending on observation

dates. We performed data reduction with the version 6.11 of the HEAsoft tools.

Figure 2 shows mosaic images of RX J1713.7–3946 which were constructed by using the data from XIS 0+1+2+3. The left and right panels show soft band (1–5 keV) and hard band (5–10 keV) images, respectively. The unit for the images is 10^{-4} counts s^{-1} pixel $^{-1}$, and the pixel size is $\sim 16.7''$. We smoothed the images using a Gaussian kernel with a FWHM of $45''$. We subtracted the non X-ray background (NXB) using **xisnxbgen**, which estimates NXB count rate based on night Earth observation data. Then, we correctet for XRT vignetting effects by simulating flat field images with **xissim** (Ishisaki et al. 2007). In the soft band image, locations of the two bright point-like sources, 1WGA J1714.4–3945 and 1WGA J1713.4–3949, are indicated by white circles. Pfeffermann & Aschenbach (1996) claimed association of the former source with a Wolf-Rayet star. The latter is thought to be a neutron star because of its X-ray spectral characteristics (Lazendic et al. 2003).

3. Analysis

3.1. Large scale CO, H α and X-ray distributions

Figure 3 shows four overlays of the $^{12}\text{CO}(J=2-1)$ distribution and X-ray images in the energy bands 1–5 keV (a, b) and 5–10 keV (c, d), respectively. A V_{LSR} range of CO from -20.2 to -9.1 km s^{-1} is shown in Figure 3 (a) and (c) from -9.1 to 1.8 km s^{-1} in Figure 3 (b) and (d), respectively. These overlays show a trend that CO and X-rays have a good correlation at a pc scale. The CO peaks (hereafter CO clumps) are identified by Fukui et al. (2003) and Moriguchi et al. (2005) except for the clumps Dw and Osw that are newly identified in the present work. It is remarkable that most of the X-ray features are found toward CO clumps with only two exceptions, one of which is toward the candidate stellar

remnant at $(\alpha_{J2000}, \delta_{J2000}) = (17^{\text{h}} 13^{\text{m}} 28^{\text{s}}, -39^{\circ} 49' 48'')$ and the other is a Wolf-Rayet star $(\alpha_{J2000}, \delta_{J2000}) = (17^{\text{h}} 14^{\text{m}} 30^{\text{s}}, -39^{\circ} 46' 00'')$. In addition, ~ 10 X-ray point sources are distributed in the pointings but no excess can be seen toward their directions in Figure 2.

We see that the correlation between the X-rays and CO is good at a scale of pc, but at finer scales of 0.1 pc the peak of a CO clump tends to be shifted from the X-ray peak. Except for the clumps C, L and Osw, which are located inside of the SNR boundary, most of the CO clumps (A, B, D, Dw, E, G, O, Q and R) are embedded on the outer boundary of the SNR shell. The observed properties of the CO clumps are listed in Table 2; column (1): clump name; (2)–(3): position of the observed point with the maximum of $^{12}\text{CO}(J=2-1)$ intensity; (4)–(6): observed properties of the $^{12}\text{CO}(J=2-1)$ spectra (radiation temperature, V_{LSR} and FWHM line width); (7)–(9): size, luminosity and mass of the clump (Moriguchi et al. 2005; Sano et al. 2010); (10) : associated *IRAS* point source.

Figure 4 (a) shows the same XIS mosaic image (1–5 keV) as Figure 2 (a), but the color scale is changed to stress the region of the low photon counts. We find the diffuse X-ray emission from the whole SNR has a good signal to noise ratio thanks to the low background of *Suzaku*. Figure 4 (b) shows the enlarged view in the SE-rim overlaid with the HI proton column density contours (white). The integration range is -20.0 – -11.0 km s $^{-1}$. The lowest contour level and the contour interval in the HI proton column density are 2.0×10^{21} cm $^{-2}$ and 0.1×10^{21} cm $^{-2}$, respectively. We apply the HI self-absorption by following a previous analysis in Paper II. It is remarkable that the distribution of the self-absorption corrected HI is complimentary to the X-ray peaks in the low-photon-count region in the SE-rim. We define a straight line PQ which passes through the center of the SNR and the X-ray peak in the SE-rim (see Section 3.2).

3.2. Detailed Comparisons with the X-Rays

In order to illustrate the observational trend in Section 3.1 we made a comparison between CO clumps and X-rays for twelve CO clumps and present the results in Figures 5. The crosses in each image indicate the center of gravity of the CO clumps listed in Table 3 columns (2)–(3), which is weighted by the CO integrated intensity, differs somewhat from the CO peak position in Table 2 columns (2)–(3). In the right panels, we plot radial profiles of the CO integrated intensity and X-ray counts for the 1–5 keV and 5–10 keV bands centered on the center of gravity. Superposed are the *Suzaku* X-ray images in 1–5 keV and 5–10 keV. The higher energy band is free of absorption and the consistency between the two energy bands indicates that the absorption is not significantly affecting the X-ray images. Each arrow indicates the direction of the center of the SNR. The dashed magenta circles represent radii of 0°06 and 0°12 around the center of gravity for each CO clump. Right panels in Figures 5 show the radial profiles around each molecular clump in the $^{12}\text{CO}(J=2-1)$ integrated intensity and the *Suzaku* two energy bands. All these features, except for the clumps D and Dw, clearly show that the X-ray emission is enhanced on the surface of each CO clump. This picture is consistent with the previous result on the clump C (Paper I). The averaged behavior is that the CO clumps have a radius of 0.04 ± 0.01 degrees and the X-rays are distributed with a separation 0.06 ± 0.03 degrees from the center of each clump (see also Table 3).

Also, we have made a comparison between HI clumps and X-rays around the SE-rim and present the results in Figure 6. The crosses indicate the HI column density peaks on a straight line PQ (Section 3.1). Radial profiles are also plotted. The trend of the relationship between HI and X-rays is similar to that between the CO and X-rays, since the HI peak trends to be shifted from the X-ray peak.

In Figure 7 top panels show the same XIS mosaic images (1–5 keV) as in Figure 4 (a)

and middle and lower panels show the azimuthal angular distribution of the X-rays around each CO and HI clump. The lines connecting the CO or HI clump positions (shown in Figures 5, 6 and Table 3) and the center of the SNR $(l, b) = (347^\circ.3, -0^\circ.5)$ or $(\alpha_{J2000}, \delta_{J2000}) = (17^h 13^m 34^s, -39^\circ 48' 17'')$ are defined as the origins of the azimuth angles, which is measured counterclockwise. The azimuthal angular distribution of the X-rays around each CO/HI clump is estimated with respect to the direction of the center of the SNR. In order to do this, we estimate the background level of the X-rays to be $\sim 66 \times 10^{-4}$ counts s^{-1} arcmin $^{-2}$, an average of the minimum value of the 1–5 keV X-ray profiles in Figure 7. This value is consistent with the nearly flat X-ray distribution inside the SNR. By setting a level at 1.5 times this X-ray background tentatively, we measured the azimuthal angular extent of the X-rays in each clump by using the 1–5 keV band image, because the signal to noise ratio is better in the 1–5 keV than in the 5–10 keV band. The results are shown in Table 3 and Figure 8. In most of the azimuth distributions of the X-rays around each clump X-rays are enhanced at the azimuthal angle 0 degrees (clumps A, B, D, Dw, E, G, O, Q, R and SE-rim). The three clumps inside the SNR, clumps C, L and Osw, are fully surrounded by the X-rays, which show a peak toward the azimuthal angle -180 degrees (clumps C and Osw) or $+120$ degrees (clump L). These distributions indicate that the clumps inside of the SNR are surrounded by the enhanced X-rays, and that those on the border of the SNR have enhanced X-rays only in the inner part of the SNR shell.

4. Discussion

4.1. Molecular and atomic clumps interacting with RX J1713.7–3946

Paper I showed that the synchrotron X-ray emission is enhanced around the CO clumps in the northwest region of RX J1713.7–3946. In the present paper, we have compared the X-rays and the molecular and atomic clumps over the whole SNR and presented a schematic

image of these results in Figure 9. This figure indicates that the X-rays are enhanced around “all the CO and dense HI clumps” within or on the outer boundary of the SNR shell. We infer that the CO clumps C, L and Osw survived the SNR blast waves because of their high density, being now embedded within the SNR. This picture is consistent with the MHD numerical simulations made by Inoue et al. (2012) that the SNR shock waves cannot penetrate into the dense clumps, and the interaction produced turbulent and enhanced magnetic field around the clumps. The other CO clumps, for instance clump A, are also X-ray brightened only toward its inner side (about ± 90 degrees in Figure 8), indicating the shock interaction only at the surface of those CO and HI clumps toward the center of the SNR. We see similar distributions of the X-rays in the high energy band (5–10 keV) that is hardly absorbed. The absorption in the X-rays therefore does not explain the depression. The morphology in Figures 7 and 8 indicates unmistakably that the X-ray emission is enhanced on the surface of the CO and HI clumps and is produced by the interaction between the SNR blast waves and each CO/HI clump. These CO and HI clumps, now interacting with the SNR blast waves, were formed over a timescale of Myr by the stellar winds of the OB star which experienced a SN explosion 1600 yr ago (e.g., Papers I and II). Thus, the density in the SNR interior is expected to be very low. The observational results also indicate that there is no dense gas left in the interior of the SNR (see also Figure 3). According to the numerical simulations, which studied the interaction of the ISM with the strong stellar wind from O-type star, the gas density inside the evacuated wind bubble is $n \sim 0.01 \text{ cm}^{-3}$ (Weaver et al. 1977). This value is significantly less than 2 cm^{-3} , obtained from the upper limit of the thermal X-rays (Takahashi et al. 2008). Therefore, the present results are consistent with that thermal X-rays has not been detected toward the inner region of the SNR.

4.2. Mechanism for the X-ray enhancement

The X-rays from the SNR RX J1713.7–3946 is purely synchrotron, which is spatially correlated well with the CO and HI clumps on a pc scale but anti-correlated on a 0.1-pc scale as described above. If the X-rays trace the shock-amplified magnetic field and CR electrons, this trend is explained naturally as the results of the interaction between the molecular and atomic clouds and the SNR. Inoue et al. (2009, 2012) carried out MHD numerical simulations of the interaction between the shock waves and the highly inhomogeneous neutral gas created by thermal instability to model RX J1713.7–3946. The shock waves in the SNR propagate to the ambient cavity with density of $< 1 \text{ cm}^{-3}$ and the CO and HI clumps having density of $\sim 10^2\text{--}10^3 \text{ cm}^{-3}$. Then the shock velocity in the dense clump becomes $V_{\text{sh,clump}} = V_{\text{sh,ambient}}(n_{\text{ambient}}/n_{\text{clump}})^{0.5}$, where the ambient density $n_{\text{ambient}} = 1 \text{ cm}^{-3}$ and the clump density $n_{\text{clump}} = 10^2\text{--}10^3 \text{ cm}^{-3}$, and the shock is stalled when it collides with a dense clump. Inoue et al. (2012) calculated that the temperature of the shocked dense gas becomes much lower than the temperature in the post-shock diffuse gas and the thermal X-ray line emission is strongly suppressed, after the shock waves passed in it (see also Section 4.3 of Inoue et al. 2012). The shock velocity difference between the dense CO/HI clump and the inter-clump ambient medium will become a factor of $\sim 10\text{--}30$. This velocity difference induces turbulence, which leads to turbulent dynamo action. As a result, the magnetic field is amplified to as high as 1 mG, which is consistent with the field strength derived from rapid time variation of the X-ray filaments (Uchiyama et al. 2007), while an alternative is that the fluctuation in the field orientation may explain the rapid time variation (Helder et al. 2012). The synchrotron flux integrated in the line of sight is proportional to $B^{1.5}$ if the spectral index of electrons p is 2.0 (e.g., Rybicki & Lightman 1979). So, it is possible to enhance the X-ray radiation around the CO and HI clumps. The observed power of the X-ray emission around the CO and HI clumps is 5–10 times higher than the inner part of the SNR. Then, the magnetic field around the CO and HI clumps is

estimated to be 3–5 times higher than in the interior of the SNR, if the difference is due to only the magnetic field amplification. Therefore, the averaged magnetic field around the CO and HI clumps becomes 45–75 μG if the initial strength is assumed to be 15 μG (e.g., Tanaka et al. 2008). The average field strength is also estimated by the width of synchrotron X-ray filaments as $\sim 100 \mu\text{G}$ (Bell 2004; Hiraga et al. 2005; Ballet 2006). Note that the dependence of the synchrotron flux on the magnetic field strength can be much more sensitive than the above-mentioned standard case, because the high-energy electrons that contribute the X-ray synchrotron emission can be in the cut-off regime (Bykov et al. 2008). Moreover, such enhanced magnetic field may lead to more efficient acceleration in the diffusive shock acceleration (DSA; e.g., Bell 1978; Blandford & Ostriker 1978) scheme.

Finally, we discuss quantitative relationship between the CO or HI clump mass and the X-ray enhancement. We estimate the clump mass (column (9) of Tabel 2) interacting with the shock wave as defined by the total CO or HI mass within the azimuth angle range of the X-rays (column (9) of Table 3) for each clump and plot it in Figure 10 as a function of the X-ray peak intensity in Figure 7. Also, we estimate the mass of the SE-rim to be $81 M_{\odot}$ on the assumption that it is a sphere of radius 1.5 pc. The result, shown in Figure 10, indicates that the correlation between the clump mass and the X-ray intensity is good with a correlation coefficient of ~ 0.84 , by excluding the lower limits for the CO mass of clumps D and O, for which mass is not given by Moriguchi et al. (2005). Therefore, the X-ray flux is considered to be roughly proportional to the interacting mass of each CO and HI clump at pc scales. This result suggests that the ISM distribution is crucial in interpreting the non-thermal X-ray distribution. More case studies of distribution of the X-rays and the ISM will be desirable to confirm this property.

5. Conclusions

We summarize the present work as follows;

1. We have shown that all the major CO and HI clumps with mass interacting with the shock wave in RX J1713.7–3946 are associated with the non-thermal X-rays. The X-rays are enhanced within ~ 1 pc of the CO and HI peaks, whereas at smaller scales down to 0.1 pc the CO peaks tend to be anti-correlated with the X-rays which decrease toward the CO and HI clumps. We have shown a quantitative relationship between the CO or HI clump mass interacting with the shock wave and the X-ray intensity. The result indicates a good correlation between the two.
2. The present findings in 1) is compared with numerical simulations of MHD in a realistic highly inhomogeneous density distribution by Inoue et al. (2009, 2012). These simulations indicate that the magnetic field is amplified around dense molecular or atomic clumps as a result of enhanced turbulence induced by the shock interaction. We interpret that thus-amplified magnetic fields enhance the X-ray intensity, which depends on the 1.5-th power of the magnetic field strength. Such enhanced magnetic field may also lead to more efficient acceleration in the DSA scheme.

NANTEN2 is an international collaboration of 10 universities; Nagoya University, Osaka Prefecture University, University of Cologne, University of Bonn, Seoul National University, University of Chile, University of New South Wales, Macquarie University, University of Sydney, and University of ETH Zurich. This work was financially supported by a grant-in-aid for Scientific Research (KAKENHI, No. 21253003, No. 23403001, No. 22540250, No. 22244014, No. 23740149, No. 23740154 (T.I.), No. 22740119 and No. 24224005) from MEXT (the Ministry of Education, Culture, Sports, Science and Technology

of Japan). This work was also financially supported by the Young Research Overseas Visits Program for Vitalizing Brain Circulation (R2211) and the Institutional Program for Young Researcher Overseas Visits (R29) by JSPS (Japan Society for the Promotion of Science) and by the Mitsubishi Foundation and by the grant-in-aid for Nagoya University Global COE Program, Quest for Fundamental Principles in the Universe: From Particles to the Solar System and the Cosmos, from MEXT. This research made use of data obtained from Data ARchives and Transmission System (DARTS), provided by Center for Science-satellite Operation and Data Archive (C-SODA) at ISAS/JAXA.

REFERENCES

- Abdo, A. A., Ackermann, M., Ajello, M., et al. 2011, *ApJ*, 734, 28
- Acero, F., Ballet, J., Decourchelle, A., et al. 2009, *A&A*, 505, 157
- Aharonian, F. A., Akhperjanian, A. G., Aye, K.-M., et al. 2004, *Nature*, 432, 75
- Aharonian, F., Akhperjanian, A. G., Bazer-Bachi, A. R., et al. 2006, *ApJ*, 636, 777
- Aharonian, F., Akhperjanian, A. G., Bazer-Bachi, A. R., et al. 2006, *A&A*, 449, 223
- Aharonian, F., Akhperjanian, A. G., Bazer-Bachi, A. R., et al. 2007, *A&A*, 464, 235
- Ballet, J. 2006, *Advances in Space Research*, 37, 1902
- Bell, A. R. 1978, *MNRAS*, 182, 147
- Bell, A. R. 2004, *MNRAS*, 353, 550
- Bertsch, D. L., Dame, T. M., Fichtel, C. E., et al. 1993, *ApJ*, 416, 587
- Blandford, R. D. & Ostriker, J. P. 1978, *ApJ*, 221, L2
- Bykov, A. M., Uvarov, Y. A., & Ellison, D. C. 2008, *ApJ*, 689, L133
- Cassam-Chenaï, G., Decourchelle, A., Ballet, J., et al. 2004, *A&A*, 427, 199
- Enomoto, R., Tanimori, T., Naito, T., et al. 2002, *Nature*, 416, 823
- Ellison, D. C., Patnaude, D. J., Slane, P., & Raymond, J. 2010, *ApJ*, 712, 287
- Ellison, D. C., Slane, P., Patnaude, D. J., & Bykov, A. M. 2012, *ApJ*, 744, 39
- Fukui, Y., Moriguchi, Y., Tamura, K., et al. 2003, *PASJ*, 55, L61

- Fukui, Y. 2008, in AIP Conf. Proc., Vol. 1085, Proc. of 4th International Meeting on High-Energy Gamma-Ray Astronomy, ed. F. A. Aharonian, W. Hofmann, & F. Rieger (Melville, NY: AIP), 104
- Fukui, Y., Sano, H., Sato, J., et al. 2012, ApJ, 746, 82
- Halzen, F. 2007, Science, 315, 66
- Helder, E. A., Vink, J., Bykov, A. M., et al. 2012, Space Sci. Rev., 173, 369
- Hiraga, J. S., Uchiyama, Y., Takahashi, T., & Aharonian, F. A. 2005, A&A, 431, 953
- Inoue, T., Yamazaki, R., & Inutsuka, S.-i. 2009, ApJ, 695, 825
- Inoue, T., Yamazaki, R., Inutsuka, S.-i., & Fukui, Y. 2012, ApJ, 744, 71
- Ishisaki, Y., Maeda, Y., Fujimoto, R., et al. 2007, PASJ, 59, 113
- Koyama, K., Kinugasa, K., Matsuzaki, K., et al. 1997, PASJ, 49, L7
- Koyama, K., Tsunemi, H., Dotani, T., et al. 2007, PASJ, 59, 23
- Lazendic, J. S., Slane, P. O., Gaensler, B. M., et al. 2003, ApJ, 593, L27
- Maxted, N. I., Rowell, G. P., Dawson, B. R., et al. 2012, MNRAS, 422, 2230
- Matsunaga, K., Mizuno, N., Moriguchi, Y., et al. 2001, PASJ, 53, 1003
- McClure-Griffiths, N. M., Dickey, J. M., Gaensler, B. M., Green, A. J., Haverkorn, M., & Strasser, S. 2005, ApJS, 158, 178.
- Mizuno, A., & Fukui, Y. 2004, in ASP Conf. Ser. 317, Milky Way Surveys: The Structure and Evolution of Our Galaxy, ed. D. Clemens, R. Shah, & T. Brainerd (San Francisco, CA: ASP), 59

- Moriguchi, Y., Tamura, K., Tawara, Y., et al. 2005, *ApJ*, 631, 947
- Nakajima, H., Yamaguchi, H., Matsumoto, H., et al. 2008, *PASJ*, 60, 1
- Pannuti, T. G., Allen, G. E., Houck, J. C., & Sturmer, S. J. 2003, *ApJ*, 593, 377
- Pfeffermann, E., & Aschenbach, B. 1996, in *Proc. Roentgenstrahlung from the Universe*, ed. H. U. Zimmermann, J. H. Trümper, & H. Yorke, 267
- Rybicki, G. B., & Lightman, A. P. 1979, *Radiative Processes in Astrophysics* (New York: Wiley-Interscience)
- Sano, H., Sato, J., Horachi, H., et al. 2010, *ApJ*, 724, 59
- Schneider, N., Stutzki, J., Winnewisser, G., & Block, D. 1998, *A&A*, 335, 1049
- Serlemitsos, P. J., Soong, Y., Chan, K.-W., et al. 2007, *PASJ*, 59, 9
- Slane, P., Gaensler, B. M., Dame, T. M., et al. 1999, *ApJ*, 525, 357
- Slane, P., Hughes, J. P., Edgar, R. J., et al. 2001, *ApJ*, 548, 814
- Takahashi, T., Abe, K., Endo, M., et al. 2007, *PASJ*, 59, 35
- Takahashi, T., Tanaka, T., Uchiyama, Y., et al. 2008, *PASJ*, 60, 131
- Tanaka, T., Uchiyama, Y., Aharonian, F. A., et al. 2008, *ApJ*, 685, 988
- Tian, W. W., Li, Z., Leahy, D. A., et al. 2010, *ApJ*, 712, 790
- Uchiyama, Y., Takahashi, T., & Aharonian, F. A. 2002, *PASJ*, 54, L73
- Uchiyama, Y., Aharonian, F. A., & Takahashi, T. 2003, *A&A*, 400, 567
- Uchiyama, Y., Aharonian, F. A., Tanaka, T., Takahashi, T., & Maeda, Y. 2007, *Nature*, 449, 576

- Uchiyama, H., Ozawa, M., Matsumoto, H., et al. 2009, PASJ, 61, 9
- Wang, Z. R., Qu, Q.-Y., & Chen, Y. 1997, A&A, 318, L59
- Weaver, R., McCray, R., Castor, J., Shapiro, P., & Moore, R. 1977, ApJ, 218, 377
- Yoshiike, S., Fukuda, T., Sano, H., et al. 2013, submitted to ApJ
- Zirakashvili, V. N., & Aharonian, F. 2007, A&A, 465, 695
- Zirakashvili, V. N., & Aharonian, F. A. 2010, ApJ, 708, 965

Table 1. Summary of the *Suzaku* archive data of RX J1713.7–3946

Pointing ID	ObsID	α_{J2000} (^h ^m ^s)	δ_{J2000} ([°] ['] ^{''})	XIS Exp. (ks)	Date	SCI
0.....	100026010	17 12 17.0	–39 56 11	69	2005 September 26	OFF
1.....	501063010	17 11 51.5	–39 31 13	18	2006 September 11	OFF
2.....	501064010	17 12 38.0	–39 40 14	21	2006 September 11	OFF
3.....	501065010	17 12 38.2	–39 22 15	22	2006 September 11	OFF
4.....	501066010	17 11 04.5	–39 40 10	21	2006 September 12	OFF
5.....	501067010	17 11 05.1	–39 22 10	21	2006 September 12	OFF
6.....	501068010	17 14 11.6	–39 40 14	21	2006 September 13	OFF
7.....	501069010	17 14 11.4	–39 22 15	18	2006 September 19	OFF
8.....	501070010	17 14 11.8	–39 58 14	21	2006 September 19	OFF
9.....	501071010	17 12 17.6	–39 18 50	21	2006 September 20	OFF
10.....	501072010	17 15 44.5	–39 40 10	20	2006 October 5	OFF
11.....	504027010	17 11 50.8	–39 31 00	62	2010 February 15	ON
12.....	504028010	17 13 14.0	–40 14 22	19	2010 February 16	ON
13.....	504029010	17 12 39.8	–40 01 50	21	2010 February 17	ON
14.....	504030010	17 15 39.0	–40 00 47	22	2010 February 17	ON
OFF1.....	100026020	17 09 31.9	–38 49 24	35	2005 September 25	OFF
OFF2.....	100026030	17 09 05.1	–41 02 07	38	2005 September 28	OFF

Note. — The details of pointing ID from 0 to 10, OFF1 and OFF2 were also shown in Takahashi et al. (2008) and Tanaka et al. (2008).

Table 2. Properties of $^{12}\text{CO}(J=2-1)$ Molecular Clumps

Name	α_{J2000} (h m s)	δ_{J2000} ($^{\circ}$ ' ")	T_{R^*} (K)	V_{peak} (km s $^{-1}$)	ΔV_{LSR} (km s $^{-1}$)	Size (pc)	L_{CO}^{\dagger} (10^2 K km s $^{-1}$ pc 2)	Mass † (M_{\odot})	<i>IRAS</i> † point sources
(1)	(2)	(3)	(4)	(5)	(6)	(7)	(8)	(9)	(10)
A.....	17 11 38.4	−39 58 46.9	6.6	−10.0	4.5	1.6	32.5	686	17082–3955
B.....	17 12 26.8	−40 05 55.5	3.3	−8.1	4.5	1.4	9.0	190	...
C.....	17 12 27.0	−39 54 58.0	7.5	−11.9	4.6	1.2	18.8	397	17089–3951
D.....	17 11 32.5	−39 30 03.9	3.3	−9.3	4.8	1.3	13.9	292	17079–3926
Dw.....	17 11 34.3	−39 32 31.2	3.1	−1.1	6.0	1.4
E.....	17 11 21.0	−39 47 24.4	4.3	−12.3	2.7	1.6	7.5	159	...
G.....	17 10 56.3	−39 45 20.6	2.8	−11.5	4.8	1.5	14.6	307	...
L.....	17 12 30.2	−39 28 14.6	3.2	−11.7	6.0	1.4	17.6	370	...
O.....	17 13 46.0	−39 26 28.6	1.2/1.9	−4.6/1.0	4.7/3.8	1.2	2.9	61	...
Osw.....	17 13 08.9	−39 36 43.2	3.5	−1.3	1.3	1.1
Q.....	17 15 11.7	−39 26 47.4	2.8	−2.2	2.8	1.4	5.1	108	...
R.....	17 15 32.0	−39 39 28.5	3.2	−3.1	2.2	1.1	3.2	67	...

Note. — Col. (1): Clump name. Cols. (2)–(3): Position of the observed point with the maximum of $^{12}\text{CO}(J=2-1)$ intensity. Cols. (4)–(6): Observed properties of the $^{12}\text{CO}(J=2-1)$ spectra obtained at the peak positions of the CO clumps. Col. (4): Peak radiation temperature T_{R^*} . Col. (5): V_{peak} derived from a single Gaussian fitting. Col. (6): FWHM line width ΔV_{LSR} . Col. (7): Size defined as $(A/\pi)^{0.5} \times 2$, where A is the total clump surface area defined as the region surrounded by values of peak integrated intensity. If the contour is unclosed, the boundary is defined as the intensity minimum between the nearby peaks. Col. (8): The CO luminosity of the clump L_{CO} estimated by $^{12}\text{CO}(J=1-0)$. Col. (9): Total mass of the clumps derived by using the relation between the molecular hydrogen column density $N(\text{H}_2)$ and the $^{12}\text{CO}(J=1-0)$ intensity $W(^{12}\text{CO})$, $N(\text{H}_2) = 2.0 \times 10^{20} [W(^{12}\text{CO})/(\text{K km s}^{-1})] \text{ (cm}^{-2}\text{)}$ (Bertsch et al. 1993). Col. (10): Associated *IRAS* point source.

† Moriguchi et al. (2005); Sano et al. (2010)

Table 3. Results of Radial and Azimuthal Distribution

Name	α_{J2000} (^h ^m ^s)	δ_{J2000} ([°] ['] ^{''})	V_{LSR} (km s ⁻¹)	Radius (degree)	Separation (degree)	Peak Intensity	Angle (Fraction) (degree), (%)	Clump Mass (M_{\odot})
(1)	(2)	(3)	(4)	(5)	(6)	(7)	(8)	(9)
A.....	17 11 39.1	-39 59 22.2	-14.5- -5.7	0.050	0.065	239.5±0.9	-90- 90, (50)	343
B.....	17 12 25.3	-40 05 37.5	-12.7- -3.6	0.050	0.025	140.9±0.6	-120- 60, (50)	95
C.....	17 12 25.3	-39 55 07.4	-16.6- -7.4	0.040	0.035	254.3±0.9	-180-180, (100)	397
D.....	17 11 31.9	-39 29 13.6	-14.2- -4.6	0.040	...	288.1±0.9	-120-150, (75)	219
Dw.....	17 11 12.8	-39 32 43.5	-7.2- 4.8	0.040	...	274.2±0.9	-120- 90, (58)	...
E.....	17 11 22.2	-39 47 34.0	-15.1- -9.8	0.050	0.025	170±2	-150- 90, (67)	106
G.....	17 10 54.5	-39 46 25.7	-16.4- -6.8	0.050	0.075	152.9±1.2	-60- 30, (25)	77
L.....	17 12 28.2	-39 28 45.9	-17.7- -5.7	0.045	0.095	257.8±0.9	-180-180, (100)	370
O.....	17 13 49.7	-39 26 54.9	-9.8- 4.5	0.040	0.095	182±2	-120- 90, (58)	36
Osw.....	17 13 22.4	-39 35 50.6	-2.7- 0.1	0.030	0.085	188±2	-180-180, (100)	...
Q.....	17 15 09.6	-39 38 48.7	-5.1- 0.3	0.040	0.025	140±2	-120- 90, (58)	63
R.....	17 15 32.4	-39 39 28.5	-5.3- -1.2	0.035	0.025	86±2	-120- 90, (58)	39
SE-rim	17 16 09.3	-40 03 10.6	-20.0- -11.0	90.3±1.1	-60- 60, (33)	27

Note. — Col. (1): Clump name. Cols. (2)–(3): Position of the center of gravity with the $^{12}\text{CO}(J=2-1)$ integrated intensity (except for the SE-rim). Cols. (4): Integration range for the estimation of the $^{12}\text{CO}(J=2-1)$ or H I (only SE-rim). (5): Radius of molecular clump defined as the radial distance from the center of gravity of CO clumps to the point where the half values of peak integrated intensity. (6) Separation of the X-ray peak intensity from each CO clump. (7) X-ray peak intensity around each clump shown in Figure 7 (unit is 10^{-4} cnt. s⁻¹ arcmin⁻²). (8) Azimuth angle extent of the X-rays (1–5 keV), which more than background level shown in the text. (9) Clump mass interacting with the shockwave defined as the total CO or H I mass within the azimuth angle range of the X-rays (1–5 keV) for each clump.

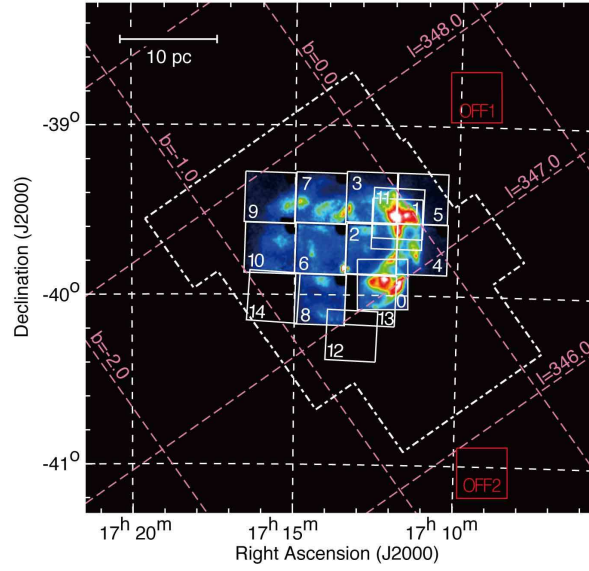


Fig. 1.— *Suzaku* FoV of each observations toward the RX J1713.7–3946 overlaid on the *Suzaku* XIS 0+2+3 mosaic image (1–5 keV) taken from Tanaka et al. (2008). The small squares correspond to the FoV of the XIS. The numbers indicated in the XIS FoV are pointing IDs used throughout this paper (see also Table 1). We also plotted observed area in the $^{12}\text{CO}(J=2-1)$ enclosed by the white dash-dotted lines.

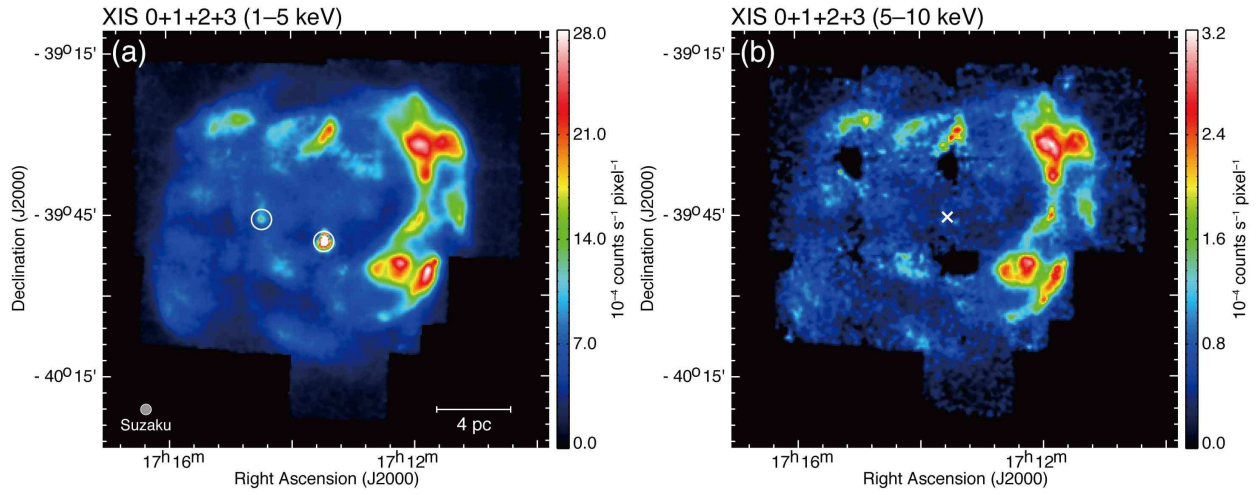


Fig. 2.— *Suzaku* XIS (XIS 0+1+2+3) mosaic images of RX J1713.7–3946 in the energy bands (a) 1–5 keV and (b) 5–10 keV. The color scale indicates count rate on a linear scale. The color bar numbers are in units of 10^{-4} counts s^{-1} pixel $^{-1}$ with a pixel size of $\sim 16.7''$. Both images are smoothed with a Gaussian of $45''$. The positions of the two point sources, 1WGA J1714.4–3945 and 1WGA J1713.4–3949, are shown with white circles (see the text).

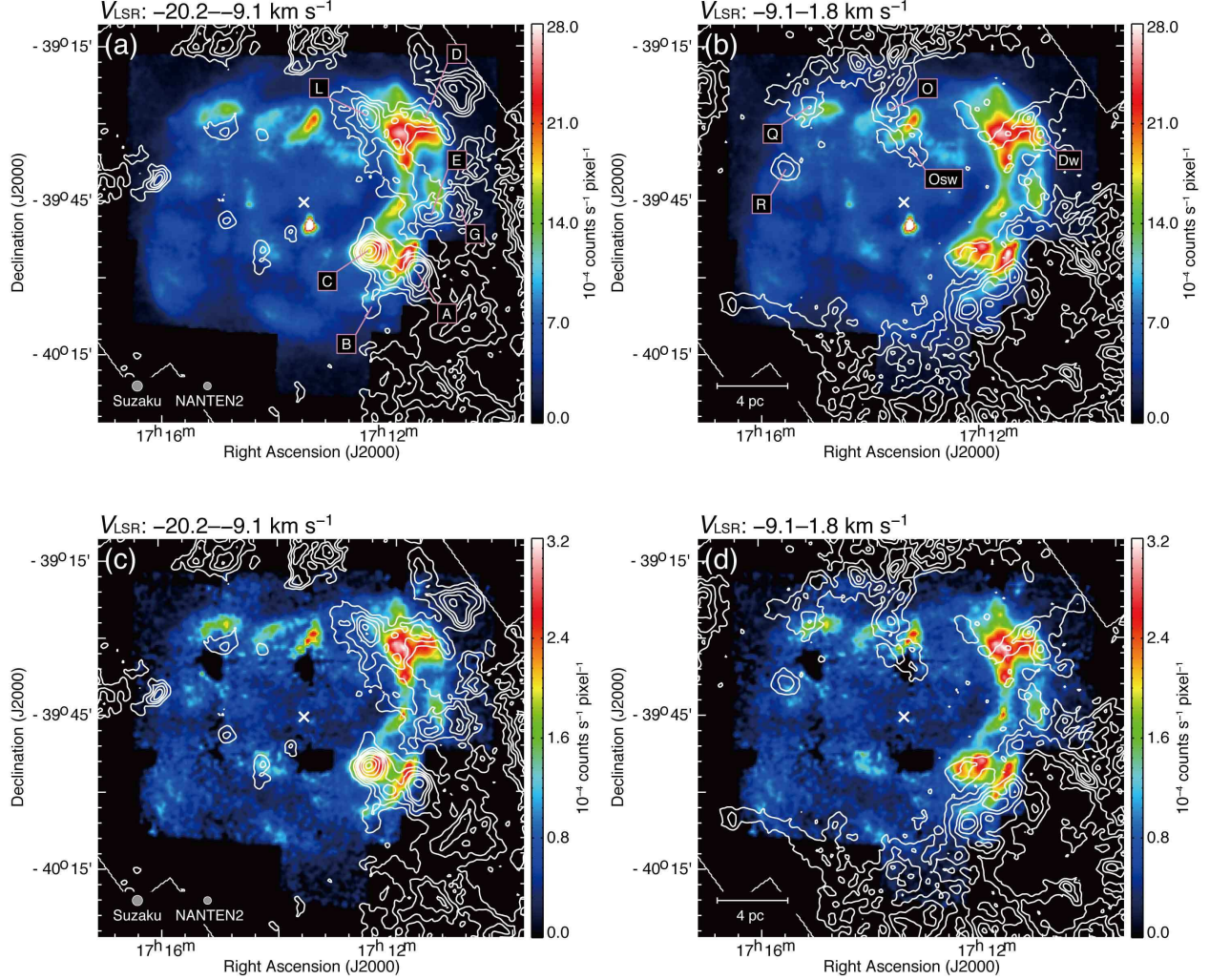


Fig. 3.— Pair of $^{12}\text{CO}(J=2-1)$ velocity channel maps (*white contours*) superposed with the *Suzaku* XIS mosaic image in two energy bands (a, b: 1–5 keV and, c, d: 5–10 keV) in color scale. The velocity ranges are (a) (c) $-20.2 \text{--} -9.1 \text{ km s}^{-1}$ and (b) (d) $-9.1 \text{--} -1.8 \text{ km s}^{-1}$, respectively. The lowest contour level and the contour interval of CO are 3.1 K km s^{-1} ($\sim 3\sigma$) in (b) and (d). In (a) and (c), the contour level are 3.1, 6.2, 9.3, 12.4, 15.5, 21.7, 27.9, 31.0 K km s^{-1} . The CO clumps, A–D, Dw, E, G, L, O, Osw, Q and R are discussed in Section 4.

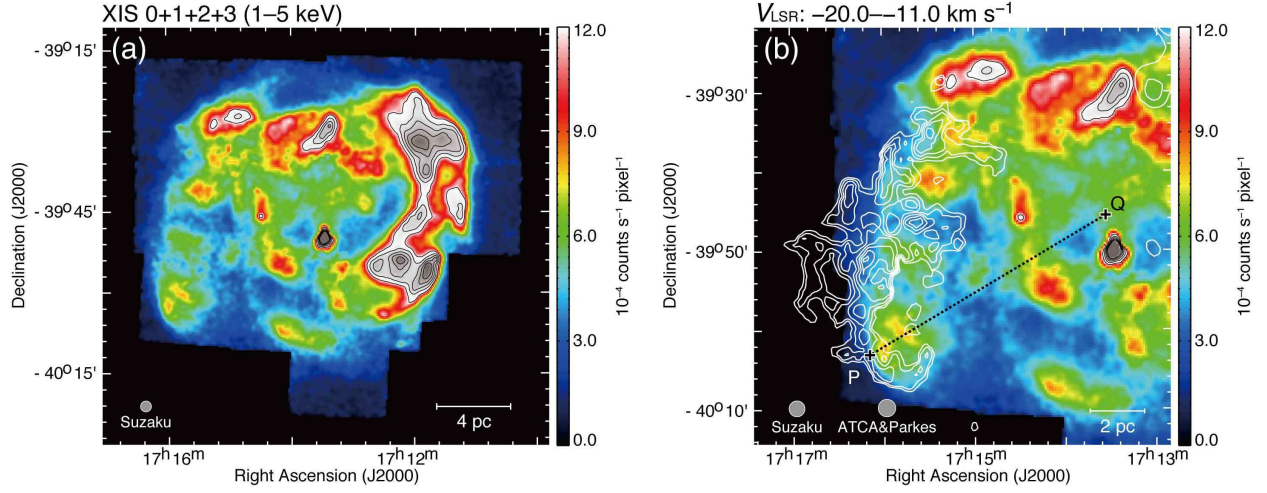


Fig. 4.— (a) Same XIS mosaic image (1–5 keV) as Figure 2 (a), but the color scale is changed to stress the region of the low photon counts. The scale is linear and units are in 10^{-4} counts s^{-1} pixel $^{-1}$. The lowest contour level and the contour interval are 3 and 1×10^{-4} counts s^{-1} pixel $^{-1}$, respectively in gray scale. This image shows X-rays by a factor of ~ 2 fainter than that in Figure 3. (b) Enlarged view in the SE-rim. The white contours indicate the distribution of HI proton column density (self-absorption corrected; see also the text and Paper II). The lowest contour level and the contour interval in HI proton column density are 2.0 and 0.1×10^{21} cm $^{-2}$, respectively. The velocity range is -20.0 – 11.0 km s^{-1} . The crosses indicate the HI column density peaks on a straight line PQ passing through the center of the SNR and the X-ray peak in the SE-rim.

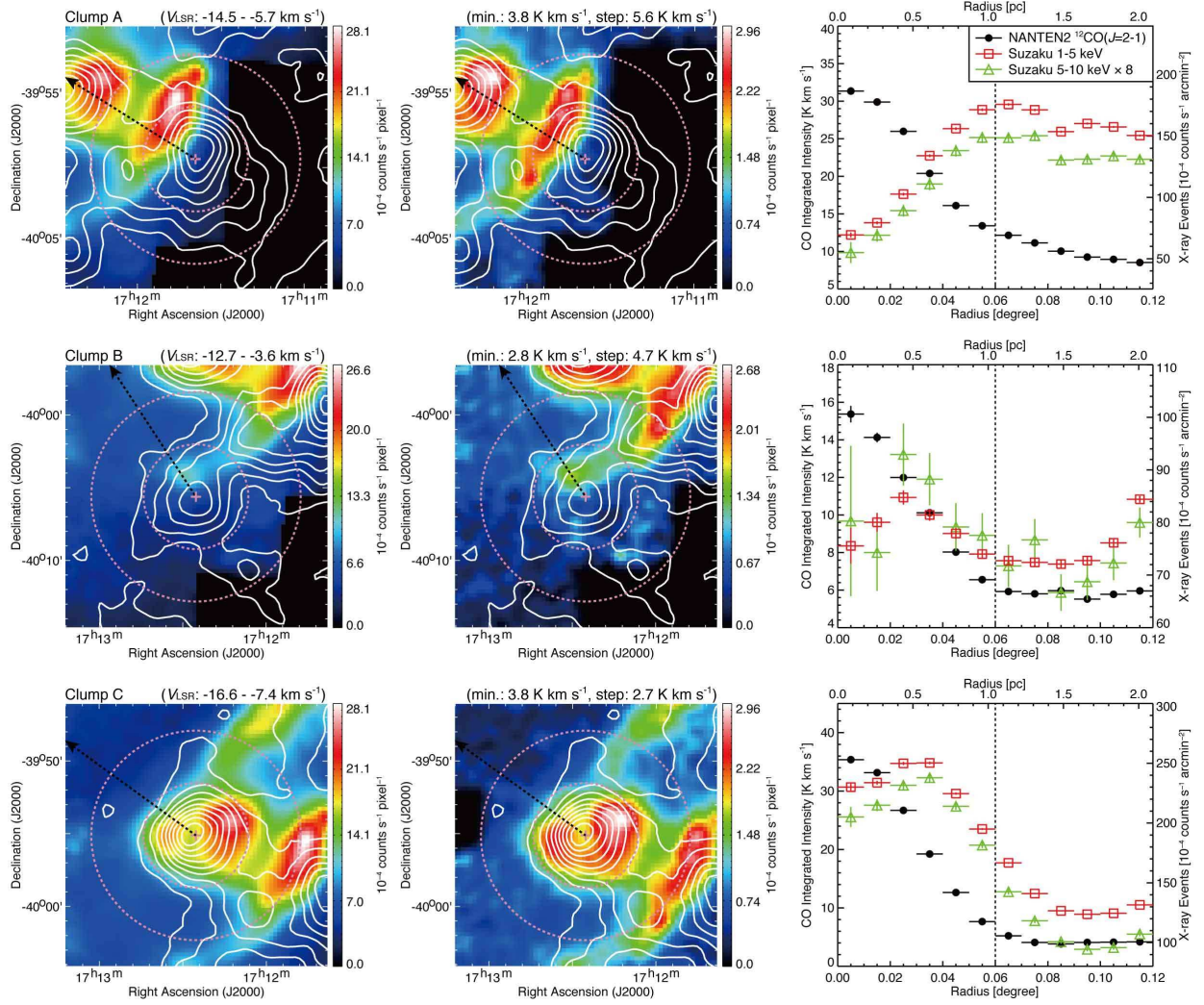


Fig. 5.— Distribution of $^{12}\text{CO}(J=2-1)$ emission (*white contours*) superposed with the *Suzaku* 1–5 keV and 5–10 keV from the left. Each CO integration velocity range and contour levels are showed in the top of the left and the middle panels, respectively. Each arrow indicate the direction of the center of the SNR. The crosses show the position of the center of gravity for the each CO clump (see also table 3). The dashed magenta circles represent radii of $0^{\circ}06$ and $0^{\circ}12$ around the center of gravity for each CO clump. Right panels show the radial profiles around each molecular clump in the $^{12}\text{CO}(J=2-1)$ integrated intensity and *Suzaku* two energy bands (1–5 keV and 5–10 keV, in units of $10^{-4} \text{ counts s}^{-1} \text{ arcmin}^{-2}$) in Figure 2. The radial profiles from the 5–10 keV band has been scaled such that it has the same area as the 1–5 keV profile (scaled by a factor 8), for direct comparisons.

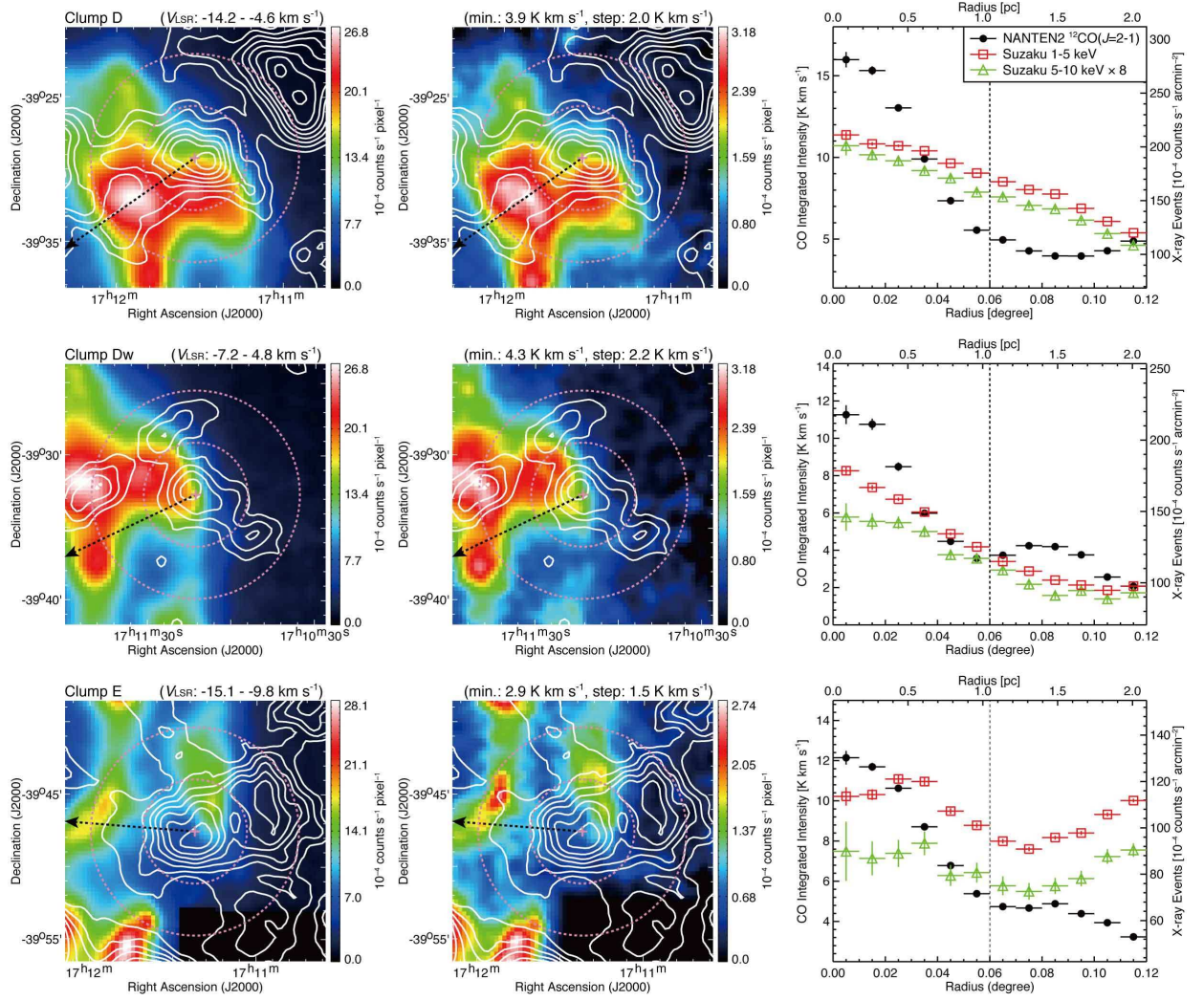


Fig. 5.— *continued*.

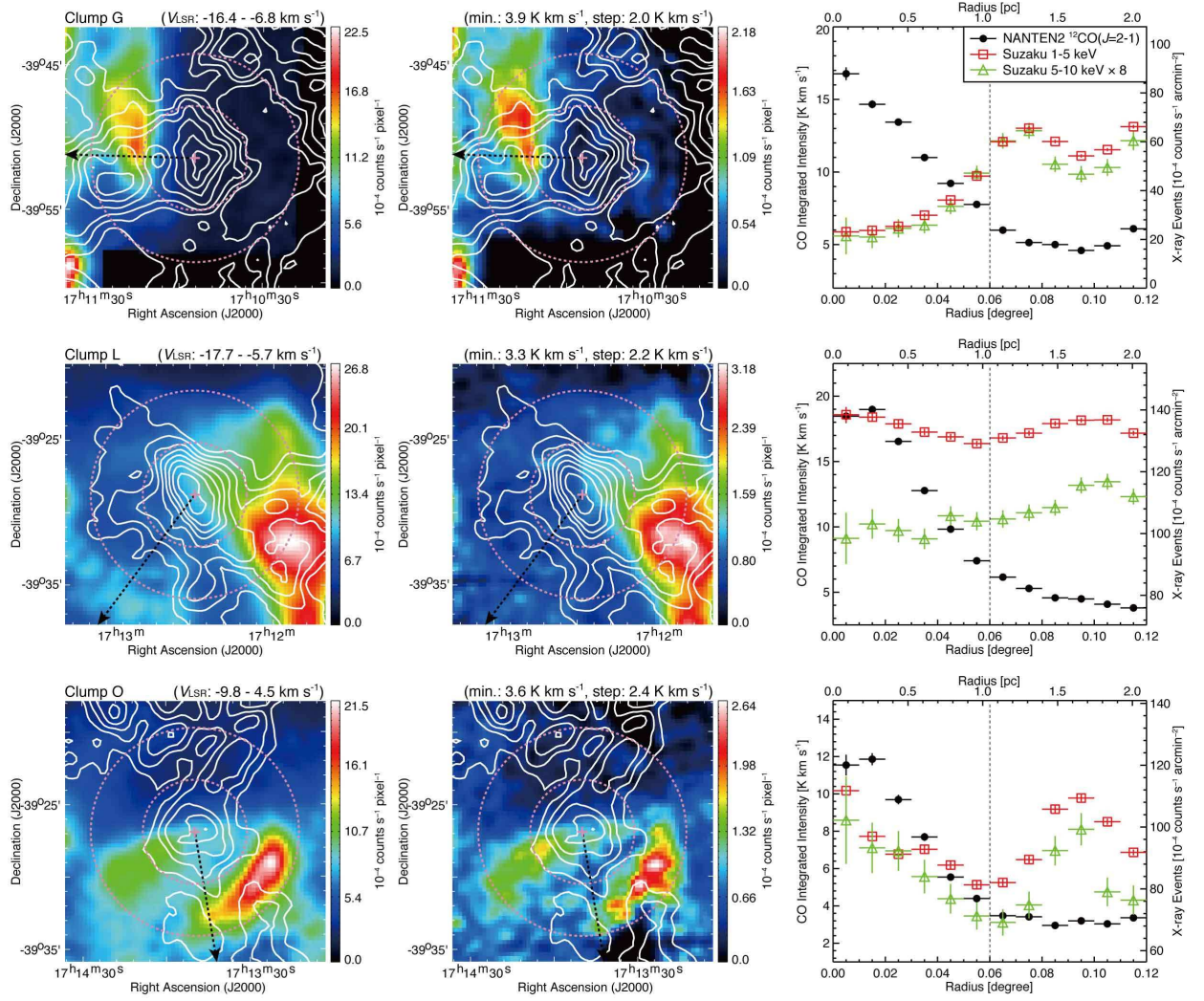


Fig. 5.— *continued.*

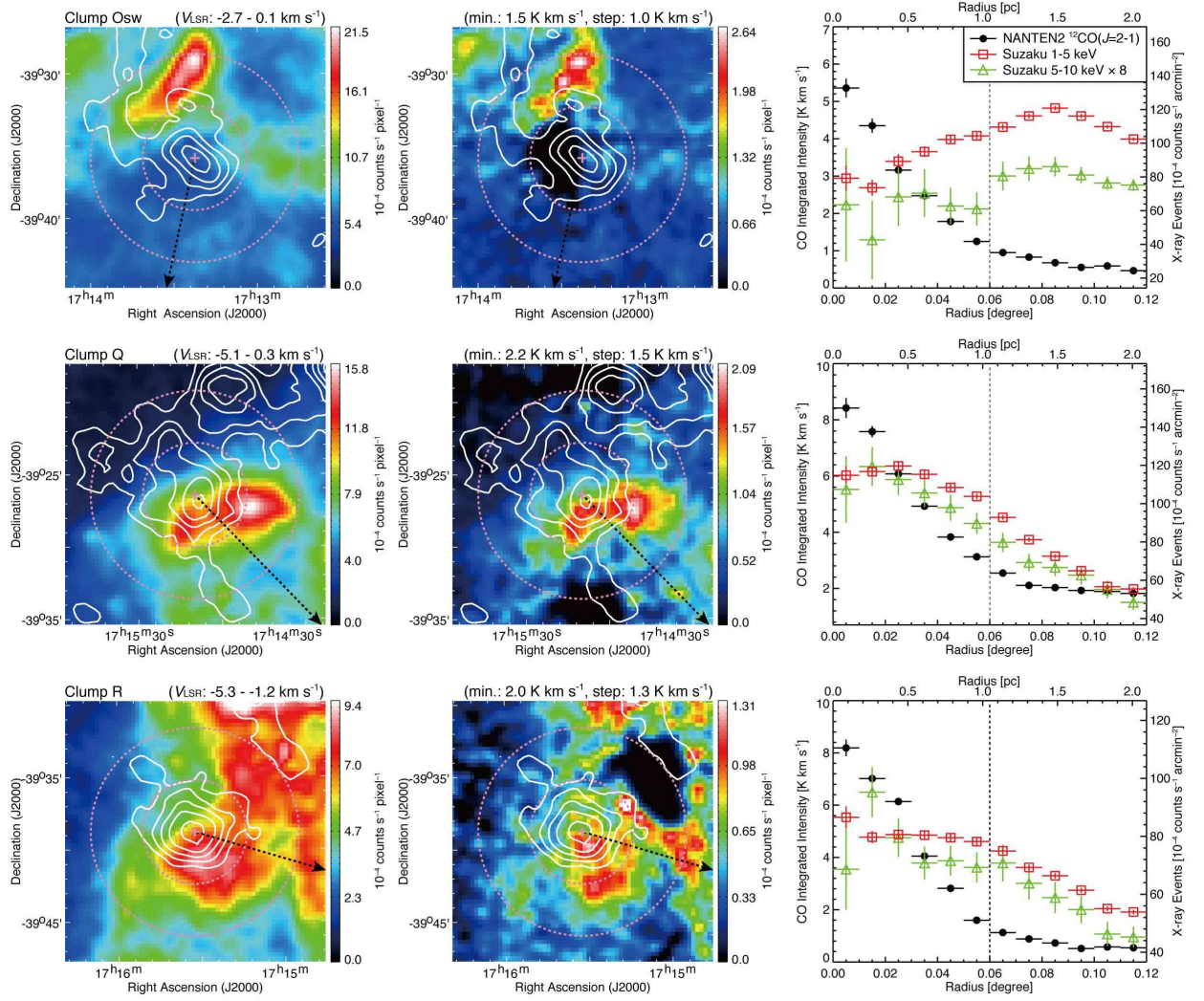


Fig. 5.— *continued.*

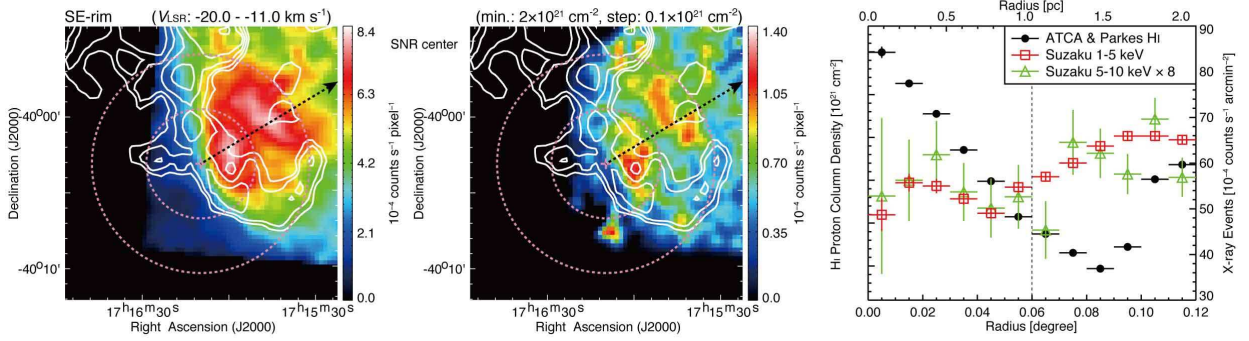


Fig. 6.— Distribution of emission HI proton column density (*white contours*) superposed with the *Suzaku* 1–5 keV and 5–10 keV from the left. HI integration velocity range and contour levels are showed in the top of the left and the middle panels, respectively. Each arrow indicate the direction of the center of the SNR. The crosses show the position of $(\alpha_{J2000}, \delta_{J2000}) = (17^{\text{h}} 16^{\text{m}} 9.3^{\text{s}}, -40^{\circ} 3' 10.6'')$ (see also table 3). The dashed magenta circles represent radii of $0^{\circ}06$ and $0^{\circ}12$ around the crosses. Right panels show the radial profiles around the crosses in HI proton column density and *Suzaku* two energy bands (1–5 keV and 5–10 keV, in units of 10^{-4} counts s^{-1} arcmin $^{-2}$) in Figure 2. The radial profiles from the 5–10 keV band has been scaled such that it has the same area as the 1–5 keV profile (scaled by a factor 8), for direct comparisons.

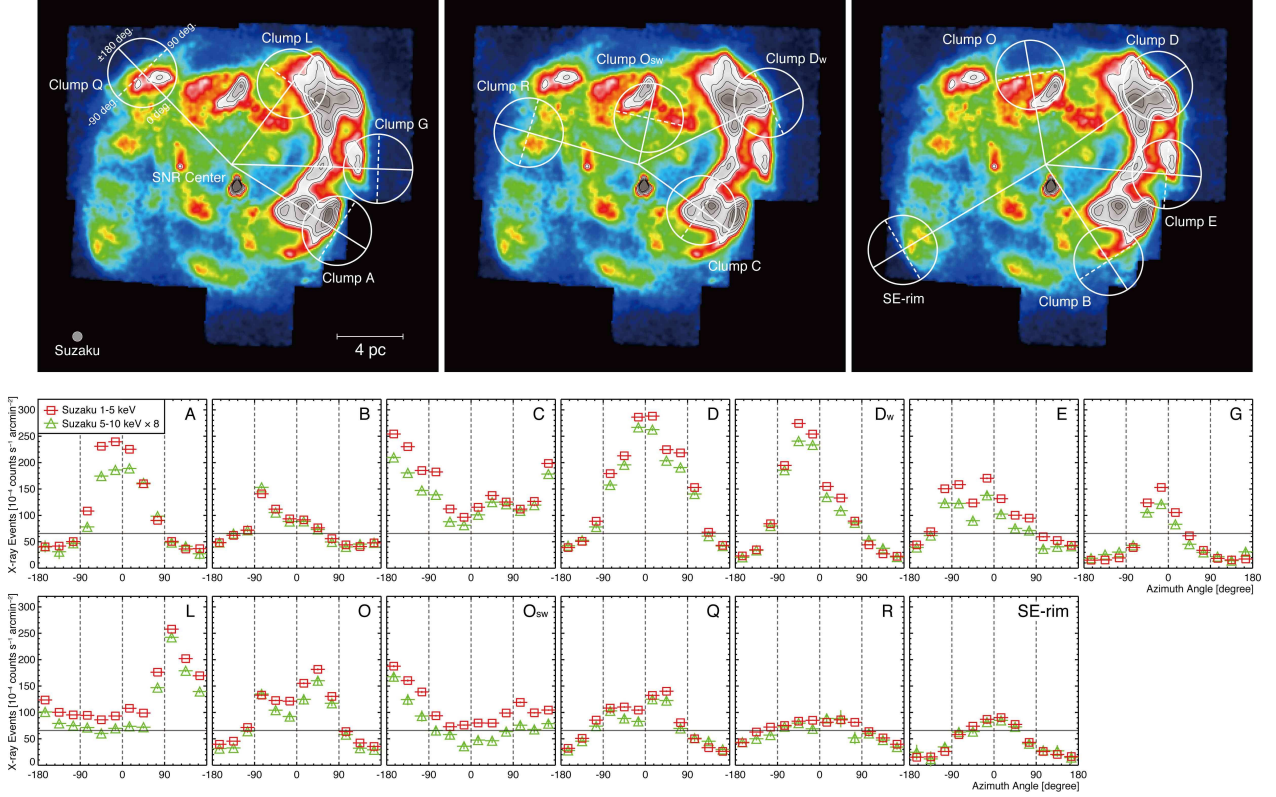


Fig. 7.— *top panels*: (a) Same XIS mosaic image (1–5 keV) as Figure 4 (a) overlaid the circles centered toward each CO/HI clump. The white circle (radius = $0^{\circ}.12$) and white lines from the center of the SNR are used for obtain the azimuth distributions shown in the lower panel. *middle and lower panels*: Azimuthal distributions of *Suzaku* XIS 1–5 keV (red square) and 5–10 keV (green triangle; scaled by a factor 8) integrated in rings centered each clump. The lines connecting the center of gravity of CO/HI clumps and the center of the SNR ($l, b = (347.3, -0.5)$) are defined as the origins of the azimuth angles. Here positive rotation is counterclockwise (e.g., clump Q in *top panel*). The horizontal solid lines indicate a background level of the X-rays (see the text).

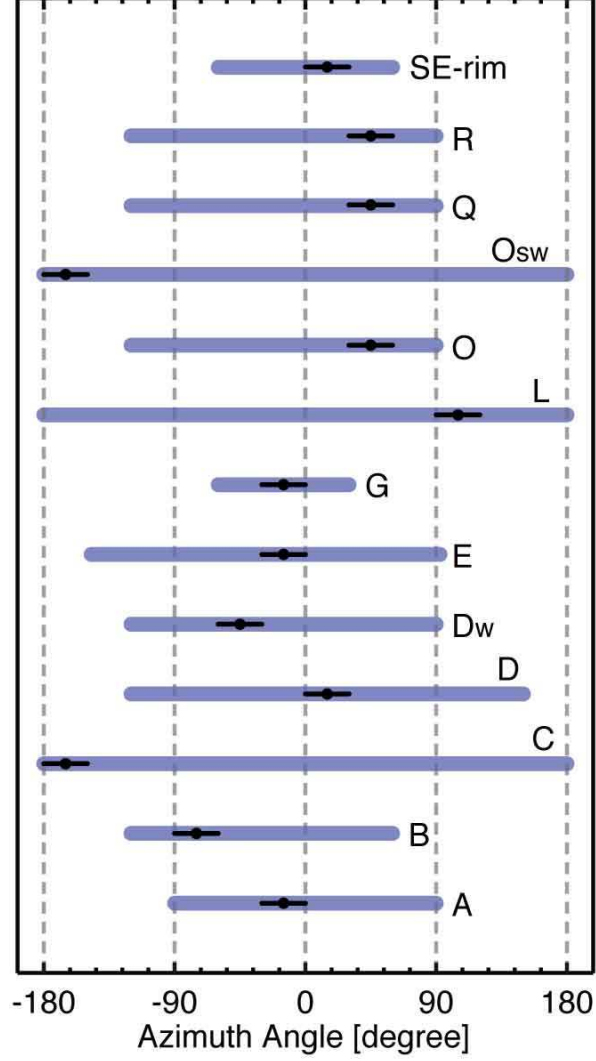


Fig. 8.— The plots of the degree of angular extent subtended by enhanced X-rays (1–5 keV band) for each CO/HI clump (see also Table 3). Each black dot indicates the angles that the X-ray peak intensities around the each molecular clump.

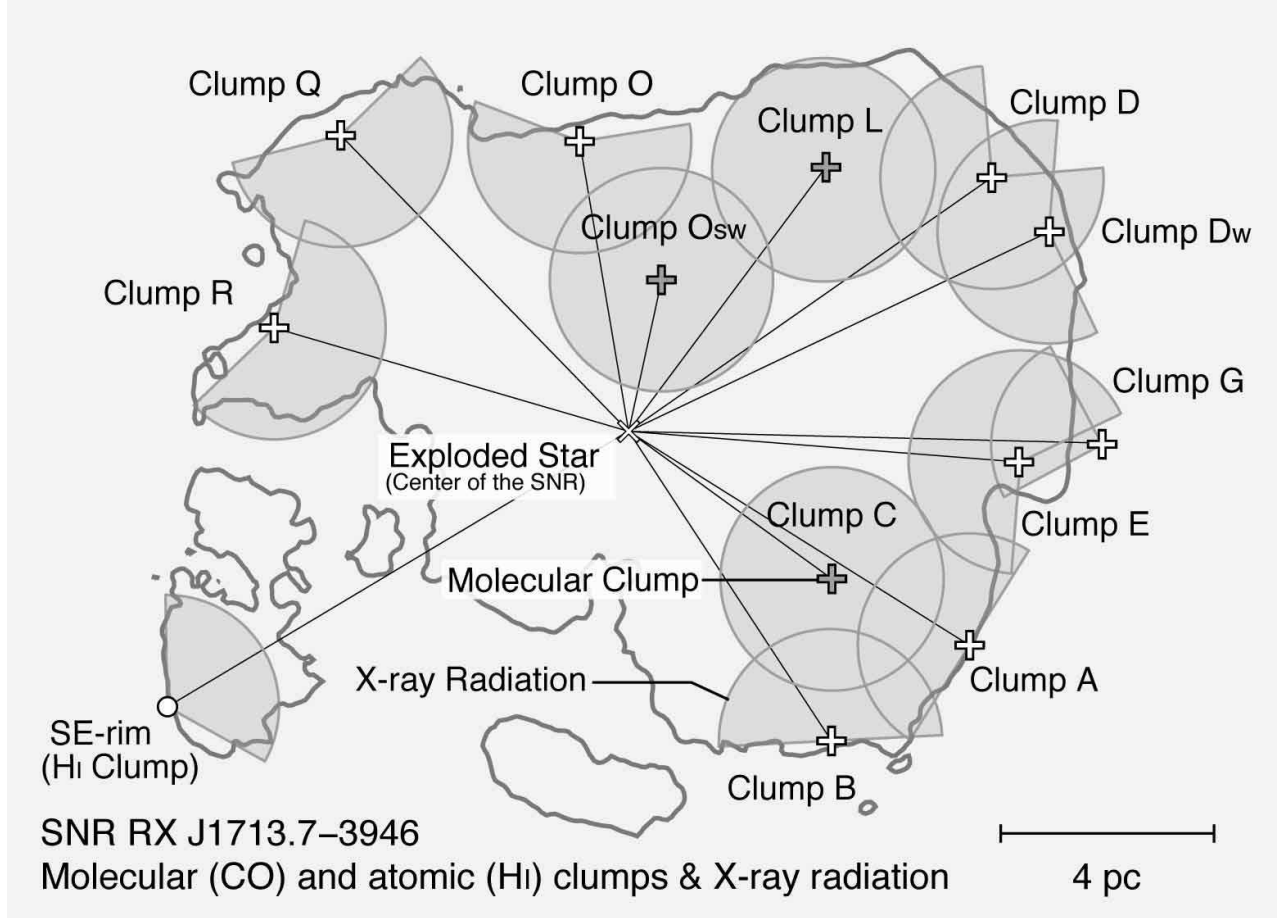


Fig. 9.— Schematic image of the distribution of the molecular (CO) clumps (open crosses), atomic (HI) clump (circle) and the X-ray radiation (shaded partial and full circles) superposed with the *Suzaku* 1–5 keV X-ray boundary line of the SNR (gray contours). The black open crosses (clumps C, L and Osw) indicate that is able to survive against the shock wave.

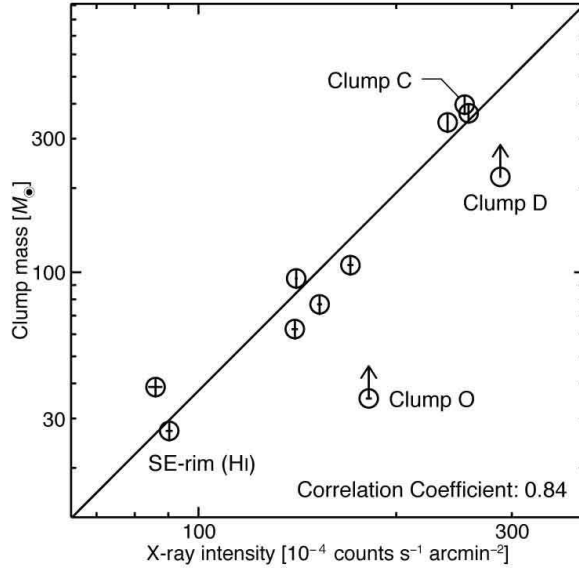


Fig. 10.— Correlation plot between the X-ray peak intensity derived by Figure 7 and the clump mass interacting with the shockwave defined as the CO or HI clumps mass within the azimuth angle range of the X-rays (column (9) of Table 3) for each clump. The plots are fitted by the method of least squares. As a result, correlation coefficient to be ~ 0.84 . We excluded the clumps D and O in the fitting (see the text).